



Achieving high energy storage performance and breakdown strength in modified strontium titanate ceramics

Mahmoud S. Alkathy^{1,*} , Fabio L. Zabotto¹, Flavio Paulo Milton¹, and J. A. Eiras^{1,*}

¹ Physics Department, Federal University of São Carlos, São Carlos, SP 13565-905, Brazil

Received: 26 March 2022

Accepted: 19 May 2022

Published online:

7 June 2022

© The Author(s), under exclusive licence to Springer Science+Business Media, LLC, part of Springer Nature 2022

ABSTRACT

Lead-free ceramic capacitors with attractive properties such as their environmental friendliness, superior energy density, fast charge and discharge rate, and superior stability have recently received increased attention to meet market demands for energy storage devices in low consumption systems. However, overcoming its relatively low energy storage capacity is becoming extremely important. Based on this task, La^{3+} and Li^{+} co-doped SrTiO_3 ceramics are fabricated by a solid-state reaction method. The effect of La^{3+} and Li^{+} contents on the structural, microstructure, dielectrics, and energy storage properties of SrTiO_3 ceramics are systematically studied. XRD confirmed the phase structure along with Rietveld refinement studies. The morphological structure is studied using SEM. Through X-ray photoelectron spectroscopy spectra, the chemical composition and the chemical state of $\text{Sr}_{(1-x)}(\text{Li}_{0.50}\text{La}_{0.50})_x\text{TiO}_3$ (SLLTx); ($0 \leq x \leq 8\%$) ceramics are studied. The energy storage properties are theoretically estimated by integrating the polarization versus electric field P-E hysteresis loop. The results show an increase in La^{3+} and Li^{+} content (x), resulting in enhanced dielectric breakdown strength, and maximum polarization yields a higher energy storage density. In the sample with $x = 8\%$, it is found that the energy density is 2.455 J/cm^3 and the energy efficiency is more than 90%. The further improvement in dielectric constant, dielectric breakdown strength, enhanced energy storage densities and the energy efficiency maintained $> 90\%$ make these materials commercially promising for energy storage device capacitors for a wide range of energy storage applications.

Address correspondence to E-mail: alkathy@df.ufscar.br; eiras@df.ufscar.br

1 Introduction

The demand for multifunctional materials increases with the rapid development of electronic, optical, and biological devices [1–3]. Due to the diverse and attractive properties of SrTiO₃ [4–6], it has become one of the distinctive ceramic materials of great interest in technological applications. Recently, SrTiO₃ meted an interest of researcher interest in the field of energy storage development due to its remarkable properties, such as relatively high dielectric constant (ϵ_r), low dielectric loss, and moderate dielectric breakdown strength (E_b) [7–9]. Despite the remarkable properties of ceramic materials, the problem of low energy storage density (W) of dielectric capacitors is a significant challenge because it is far inferior to other energy storage devices such as supercapacitors and batteries. In terms of theoretical physics, and based on the following formula, there are two options to enhance the energy storage density (W) of ST ceramics capacitors by increasing its dielectric constant (ϵ_r) or its breakdown strength (E_b).

$$W = \frac{1}{2} \epsilon_0 \epsilon_r E_b^2, \quad (1)$$

where (ϵ_0) is the dielectric constant of the free space. Many researchers have reported enhancing the dielectric permittivity in some doped and co-doped SrTiO₃ ceramics [10–20]. For example, Zhong et al. [10] obtained a colossal dielectric permittivity in co-doping SrTiO₃ ceramics by Nb and Mg. Qin et al. [11] reported that the point defect structure induced by La-doped SrTiO₃ ceramics leads to colossal permittivity. Also, Guo, Xu et al. [12] reported that the doped of La on the Sr site of SrTiO₃ induced a colossal permittivity that can be utilized to enhance the energy storage capacitors. Defect chemistry and colossal dielectric behaviour of Nd-modified SrTiO₃ lead-free ceramic materials were also reported by Guo, Xu et al. [14]. Alkathy et al. [19] also reported a colossal dielectric permittivity and high energy storage efficiency in barium strontium titanate ceramics co-doped with bismuth and lithium. On the other hand, the enhancement of breakdown strength (E_b) was also reported by several researchers [21–25]. For example, Zhong et al. [21] are found that doped SrTiO₃ with 0.2% Eu³⁺ exhibit high breakdown strength up to 354 kV/cm and a relatively high recoverable energy density of 2.13 J/cm³. Zhu et al.

[22] reported the enhancement of energy storage density of SrTiO₃ lead-free relaxor ceramics via doped Bi at that induced A-site defect and grain size tuning. Pu et al. introduced Zr⁴⁺ into Ca_{0.5}Sr_{0.5}TiO₃ ceramics to suppress grain growth, and the barrier effect at grain boundaries is enhanced by annealing in oxygen. Finally, a high E_b of 440 kV/cm was obtained [23]. Pan prepared SrTi_{0.985}(Zn_{1/3}Nb_{2/3})_{0.015}O_{3-x}wt%ZnNb₂O₆ ceramics through synergy manipulation and brought a high E_b of 422 kV/cm and an energy storage density of 2.35 J/cm³ [24]. In particular, Dy-doped SrTiO₃ obtains a high recoverable energy density of 4.00 J/cm³ and an extremely high breakdown strength of 510 kV/cm through oxygen treatment and increasing the resistance of crystal grains and grain boundaries [25]. According to reports on high dielectric constants in single-doped STO, co-doping may provide more freedom to control the dielectric properties due to the effects of charge, lattice distortion, and defect dipoles [21, 26, 27]. Numerous studies have been conducted on solid dielectric materials for energy storage applications that offer high energy storage density, high energy efficiency, and good stability in the last few decades. In Fig. 1, we compare the energy storage properties of our study with another lead-free energy storage ceramic reported in the recent year [28–41].

This work focuses on the successful synthesis of functional, high dense La³⁺ and Li⁺ co-doped SrTiO₃

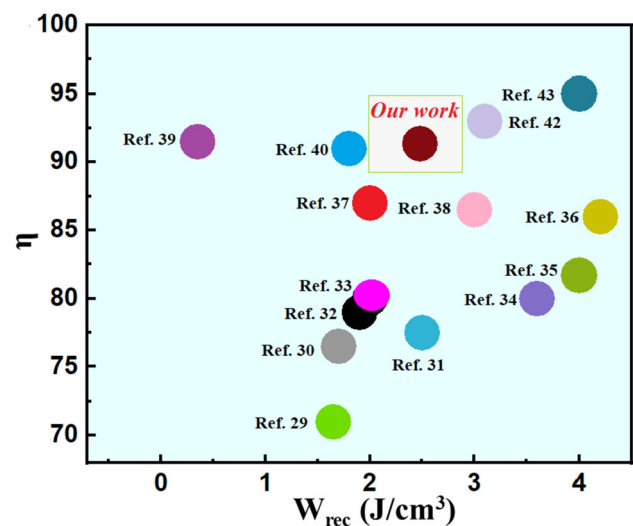
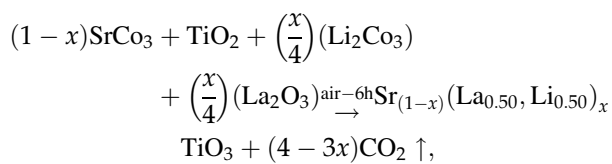


Fig. 1 A review of the energy storage properties of modified SrTiO₃ ceramics and other lead-free ceramics that are promising in the field of energy storage applications

ceramics using solid-state reaction processing. Co-doping of La³⁺ and Li⁺ has been chosen in this study to tune the electronic properties and dopant populations effectively. This technique enhances the dopant solubility, and defects with desired properties are made more stable, affecting the energy storage properties. The results of this work show an energy storage density of 2.55 J/cm³ with high energy efficiency exceeding 90%. We guess that the La³⁺ and Li⁺ co-doped SrTiO₃ can be considered promising materials for energy storage applications.

2 Experimental

La³⁺ and Li⁺ co-doped SrTiO₃ ceramics were prepared using SrCO₃, Li₂CO₃, and La₂O₃, (Sigma-Aldrich, 99.99% purity) and TiO₂ (Sigma-Aldrich, 99.98% purity). The general formula for the synthesis of the samples is:



where (0 ≤ x ≤ 0.08). The powders were mixed by ball milling for 10 h to achieve uniform mixing. The mixed powder was calcined at 1000 °C using an oven furnace with a dwell time of 6 h and heating and cooling rates of 5 °C/min. After calcination, the samples were ground well in an agate mortar for 1 h. Fine calcined powders were prepared by adding 1% PVA as a binder to form disk-shaped pellets (10 mm diameter and 1.5 mm thickness) using a pressure of 100 MPa. The green pellets were heated to 500 °C at a heating rate of 2 °C/minute to evaporate the binder. The pellets were sintered for a dwell time of 4 h at a temperature of 1300 °C in a conventional furnace. Phase confirmation was carried out using X-ray diffraction (XRD) with an X-ray diffractometer (D8-Advance) using Cu Kα radiation (40 mA, 45 kV, and λ = 1.5406 Å) at room temperature, and the analysis was carried out in a 2θ range of 20°–80°. The JCPDF program was used for the profile mapping of the phase structure of the sample. Scanning electron micrographs were taken using a scanning electron microscope FE-SEM. The binding energies were analyzed by XPS using a PHI 5000 Versa Probe II (ULVACPHI Inc., USA) equipped with a micro-

focused (200 μm, 15 kV) monochromatic Al-Kα x-ray source (hν = 1486.6 eV). The silver paste was applied to both surfaces of the sintered pellet to determine the electrical properties. Frequency-dependent dielectric constant measurements were performed using an Agilent 4294A impedance analyzer (40 Hz to 1 MHz). The samples were polished, and the thickness was decreased to 0.32 mm to investigate the P–E hysteresis loops. The measured frequency was 10 Hz, and the measured process was done in silicon oil using a homemade setup based on a sawyer–tower circuit.

3 Results and discussion

3.1 Phase characterization

Figure 2 shows the XRD pattern for Sr_{1-x}(Li_{1/2}, La_{1/2})_xTiO₃(SLLT:x), where (0 ≤ x ≤ 0.08) ceramics. The obtained results indicated that all sintered samples possess a single-phase with cubic structure, Pm3m space group, which matches the standard card for SrTiO₃ (JCPDS Card No. 35-0734) [42]. No trace of a secondary phase is detected in all investigated sintered ceramics. The structural refinements were carried out to investigate the effect of La³⁺ and Li⁺ co-doping on sintered samples' structural properties, as shown in Fig. 3a. The peaks were fitted using the pseudo-Voigt function. The obtained parameters such as lattice constant, unit cell volume, theoretical density, and R-factors of the studied samples are summarized in Table 1. Figure 3b shows that the

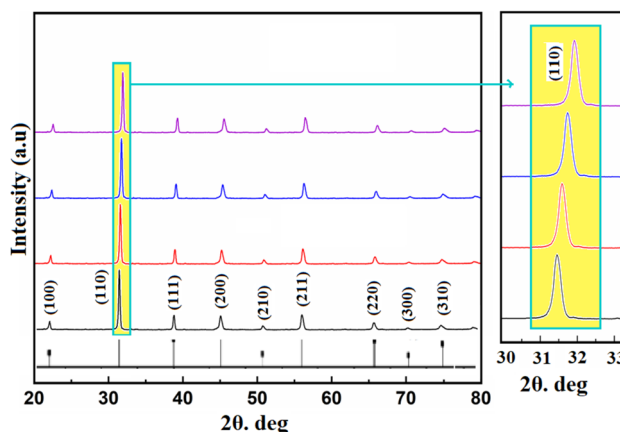


Fig. 2 XRD patterns of Sr_{1-x}(Li_{1/2}, La_{1/2})_xTiO₃ (SLLT:x) ceramics with (0 ≤ x ≤ 0.08), the right graph present an enlarged XRD patterns from 2θ = 30 (°) to 2θ = 33 (°)

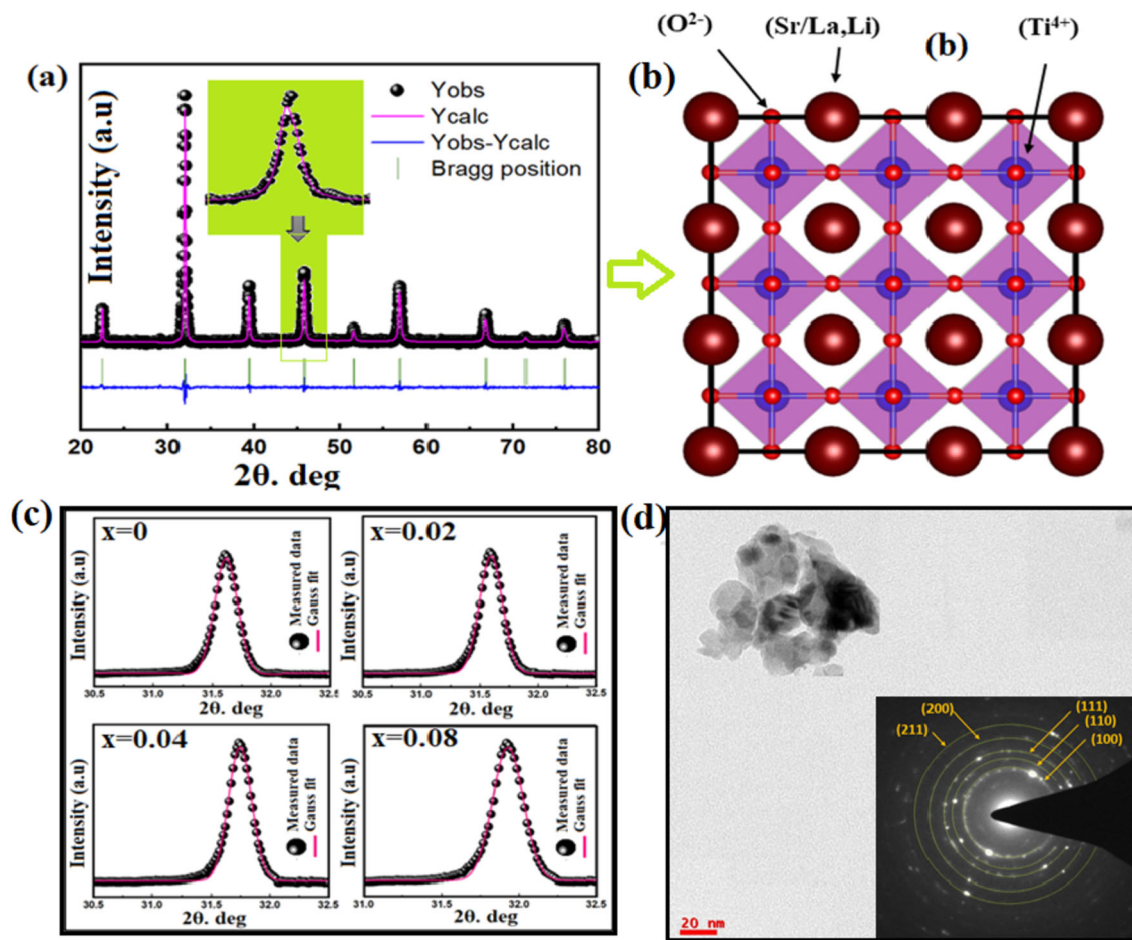


Fig. 3 Rietveld analyses of the XRD pattern show a good agreement between the observed and calculated intensities and give a clear indication of the specific phase of Pm3m for SLLT:x,

b schematic structure diagram of Cubic ST, and **c** Gaussian fitting of the 110 peaks, and **d** high-resolution TEM images of SLLT0.08 sample

Table 1 Results of rietveld refinement and Gaussian fitting of X-ray diffraction data of for SLLT x ceramics investigated at room temperature

Sample	ST	SLLT:0.02	SLLT:0.04	SLLT:0.08
Crystal system	Cubic	Cubic	Cubic	Cubic
a (Å)	3.9055	3.9042	3.9031	3.9011
V (Å) ³	59.57032	59.51085	59.46057	59.36921
Space group	Pm3m	Pm3m	Pm3m	Pm3m
SG No	221	221	221	221
Theoretical Density g/cm ³	6.12	6.08	6.1	6.11
Measured density g/cm ³	5.511	5.541	5.774	5.883
Relative density (%)	90	91	95	96
R_p	8.91	8.21	8.37	9.18
R_{wp}	11.7	11.2	11.1	11.4
R_{ex}	9.83	7.87	8.33	8.92
χ^2	1.42	2.02	1.78	1.63
FWHM (°)	0.187	0.195	0.212	0.227
Peak positions (°)	31.66	31.71	31.77	31.89
Crystallite size (nm)	46.14	44.25	40.71	38.03
Lattice strain	0.0029	0.0030	0.0033	0.0035

SLLT sample is a cubic arrangement of BO_6 octahedra units linked together by shared oxygen ions at the corners. From the reported data in Table 1, we can be seen that the lattice parameters and unit cell volume significantly decrease with an increase in La^{3+} and Li^+ concentrations. This decrease could be caused by the difference in ionic radii of dopants and host lattice. By considering the 6-coordination number of Sr^{2+} , Li^+ and La^{3+} , Shannon [43] reported that the ionic radii of $\text{Sr}^{2+}(\text{VI}) = 1.18 \text{ \AA}$, $\text{Li}^+(\text{VI}) = 0.76 \text{ \AA}$, and $\text{La}^{3+}(\text{VI}) = 1.032 \text{ \AA}$. Incorporating small ionic radii (La^{3+} , Li^+) in place of large ionic radii leads to shrinkage of the unit cell volume. This observation can confirm that the La^{3+} and Li^+ ions were successively substituted on the Sr site of the SrTiO_3 lattice. The (110) diffraction peaks were chosen and fitted using Gaussian fitting as represented in Fig. 3c. We obtained the peak (θ_c) position and full width half maximum (FWHM) from the fitting. The crystallite size and lattice strain were also estimated via Scherrer [44] and Williamson-Hall formulas [45], respectively. The crystallite is irregular in shape on the TEM image (Fig. 3d). The HRTEM image of the sintered SLLT0.08 sample and the corresponding apprehensive lattice plane are shown in Fig. 3d.

3.2 Microstructure observation

Figure 4 shows the micrograph images of SLLT: x sintered ceramics. The observed grains have varying sizes, shapes, and grain size distributions. The density of the investigated samples is obtained by the Archimedes approach [46], and the obtained values are reported in Table 1. The grain sizes were estimated using the image j software, and the obtained grains size was found to be 1.64 μm , 1.313 μm , 1.221 and 0.921 μm , with an increase in the La^{3+} and Li^+ concentrations from $x = 0$ to $x = 8\%$, respectively. The decrease in grain size could be due to the restrictions of grain growth with the incorporation of La^{3+} and Li^+ in the ST lattice. The La^{3+} and Li^+ ions might be segregated at grain boundaries, leading to regional grain growth by resisting grain boundary movement due to the interaction between the sintering additive and the SrTiO_3 -based ceramic, which reduces grain size [47]. Another reason for grain growth inhibition may be caused by the smaller ionic radius of La^{3+} and Li^+ , and a further increase of La^{3+} and Li^+ content affects grain size and shape in SLLT samples [48]. A similar observation was

reported by Yadav et al. [49, 50] in a rare-earth element. La-doped BT ceramics decrease the average grain size and are attributed to the lower diffusivity of the rare-earth elements during grain growth.

3.3 XPS study

To measure the elemental composition and binding states of the surface of the selected sample, X-ray photoelectron spectroscopy (XPS) is used. The XPS survey spectrum of SLLT:4% is shown in Fig. 5a. The survey spectra show a typical spectrum of Sr, Ti, O, La, Li and C elements. C 1s at 267.35 eV indicates the sample holder's carbon tap, and it was used to calibrate the other element-binding energies. The high-resolution spectra along with Lorentz fitting of Sr 3d, Ti 2p, O 1s, La 3d, and Li 1s, are presented in Fig. 5b–f. The XPS spectra of Sr 3d in Fig. 5b show a pair of spin-orbit split doublets (Sr 3d_{5/2} and Sr 3d_{3/2}); the dominant spectra (Sr 3d_{5/2} at 131.70 eV) correspond to primary STO lattice, while the weaker spectra, with a somewhat higher binding energy (Sr 3d_{3/2} at 133.39 eV) are attributed to the strontium oxide crystallites [51]. The Ti 3p peak spectra consist of $\text{Ti}^{4+}2p_{3/2}$ located at 456.94 eV and $\text{Ti}^{4+}2p_{1/2}$ located at 462.74 eV, and these bonding energies are matched with reported data of TiO_2 [52]. Additionally, the spin-orbital splitting energy between two spectra, $\text{Ti}^{4+} 2p_{3/2}$ and $\text{Ti}^{4+}2p_{1/2}$, is 5.8 eV, confirming the Ti^{4+} oxidation state [52]. Figure 5c shows that there is no signal identical to that of Ti^{3+} , which may result from low Ti^{3+} concentrations. Figure 5d shows the XPS spectra of O 1s, consisting of the principal peak at 528.33 eV and the shoulder spectra located at 529.77 eV. The peak spectra at 528.33 eV correspond to an oxygen lattice in the Ti–O bond [53], while the peak spectra at 529.77 eV indicated oxygen vacancies [54, 55]. Figure 5e shows the XPS spectra of La 3d. The peak of La 3d_{5/2} located at 835.33 eV and La 3d_{3/2} at 839.67 eV could be seen with an interval of 4.34 eV, which is characteristics of La_2O_3 assigned to La^{3+} [56]. Figure 5f shows Li 1s spectrum. This peak posited at 56.02 eV, which is indicated to be lithium carbonate, confirming the Li^+ state [57].

The concentrations of oxygen vacancies were estimated by taking the ratio of (OII/OI) and it is found to be 0.214. Therefore, it is concluded that the co-doped ceramic shows the significant amount of oxygen vacancies which might be resulting from the valance differences between La^{3+} , Li^+ and Sr^{2+} . In

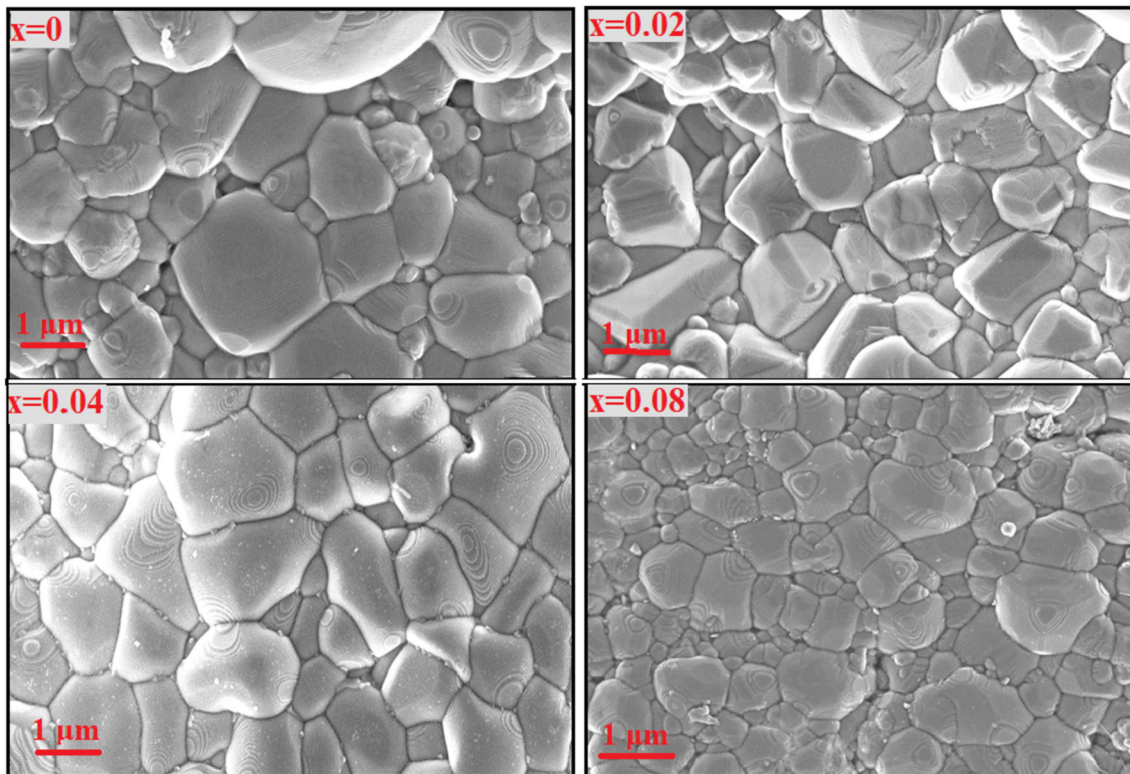
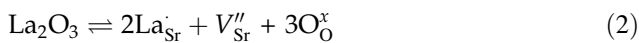
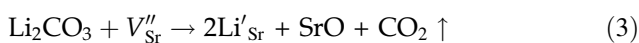


Fig. 4 SEM images of the thermally etched surface of $\text{Sr}_{1-x}(\text{Li}_{1/2}, \text{La}_{1/2})_x\text{TiO}_3$ (SLLT: x) ceramics with ($0 \leq x \leq 0.08$)

principle the La^{3+} ions substituted for the Sr^{2+} ions act as donors and the Li-ions act as acceptors under normal oxidation conditions. Physically, La^{3+} is composed of 57 electrons that revolve around the nucleus. In this case, the chemical configuration is $[\text{Xe}] 5d1 6s2$, which means the valence shell has three electrons correspondingly [58, 59]. Two electrons in the 5d subshell and one electron in the 6s subshell from the +3-oxidation state are responsible for its properties. According to the Kroger-Vink notation, the Sr^{2+} doped La^{3+} , defect is compensated by the vacancies created in the lattice of SrTiO_3 [60, 61].



Furthermore, replacing monovalent Li^+ with divalent Sr^{2+} resulted in an excess of hole carriers in the neutral Sr [62, 63]:



As shown in the dielectric discussion section, oxygen vacancies confirmed by the XPS study are crucial to producing a high permittivity, which may help improve energy storage properties.

3.4 Dielectric study

Figure 6a, b shows the frequency-dependent of dielectric permittivity and loss tangent of the (SLLT: x) ceramics with ($0 \leq x \leq 0.08$). This measurement was measured at room temperature in the 20 Hz to 2 MHz frequency range. From Fig. 6a it can be seen that the dielectric constant of the pure ST sample decreases sharply with an increase in frequency and reach to saturation state at a frequency beyond 10^4 Hz. While the dielectric constant of co-doped samples is slightly decreased before going 1 kHz, 1.8 kHz and 6 kHz for SLLT0.02, SLLT0.04 and SLLT0.08, respectively. With an increase in frequency, the dielectric constant after the frequency mentioned above is sharply reduced, and correspondingly the dielectric loss shows a sharp increase to > 0.05 . The high value of dielectric constant at frequency $< 10^3$ Hz is probably attributed to the Maxwell–Wagner type interfacial polarization or space charge contribution at the grain boundaries [64, 65]. The decrease of the dielectric constant at a higher frequency may be attributed to reducing the

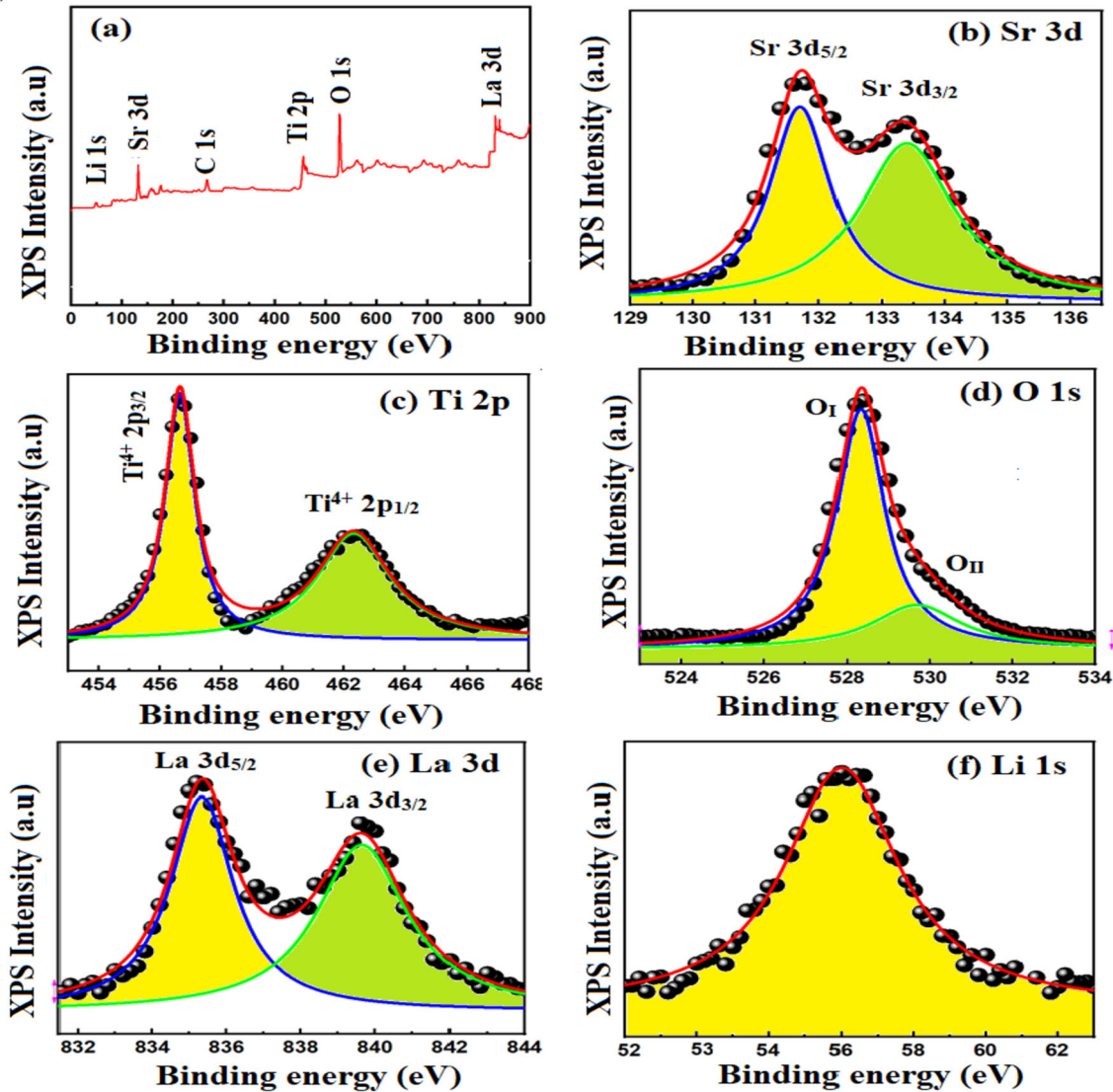


Fig. 5 a XPS survey spectra, b–f High-resolution XPS spectra of Sr 3d, Ti 2p, O 1s, La 3d, and Li 1s, respectively, of the (SLLT:4%) sintered ceramics

space charge polarization effect [64, 65]. The presence of frequency-dependent electrical relaxation phenomena in this material is shown by the prominent emergence of the peaks in Fig. 6b as frequency increases. It can be seen that the dielectric constant at 1 kHz is found to be 244, 507, 651, and 782 for SLLT0, SLLT0.02, SLLT0.04 and SLLT0.08, respectively. To explain the reason, let us consider the charge compensation mechanism. The La^{3+} ions act as donors, while the Li act as acceptor dopants; thus, a defect can be expected in the ST lattice. According to the previous literature reports [11], La^{3+} doping creates $\text{La}_{\text{Sr}} + V_{\text{Sr}}'' + \text{La}_{\text{Sr}}$ and Schottky defects in ST lattice resulting in defect dipole formation [11]. As a result

of the increase in co-dopant content, the content of defect dipoles rises, causing the dielectric constant to rise. Interestingly to see that the dielectric loss of all compositions is lower than that of pure ST compounds, which is a helpful attribute for developing future energy storage capacitor devices.

It is known that polycrystalline materials consist of grains and grain boundaries, which can play an essential role in controlling electrical properties. The ability of complex impedance analysis to discriminate between grain and grain boundaries resistance is well recognized. Impedance spectroscopy is a helpful technique that can estimate grain and grain boundaries' R and C values in several electroceramics using

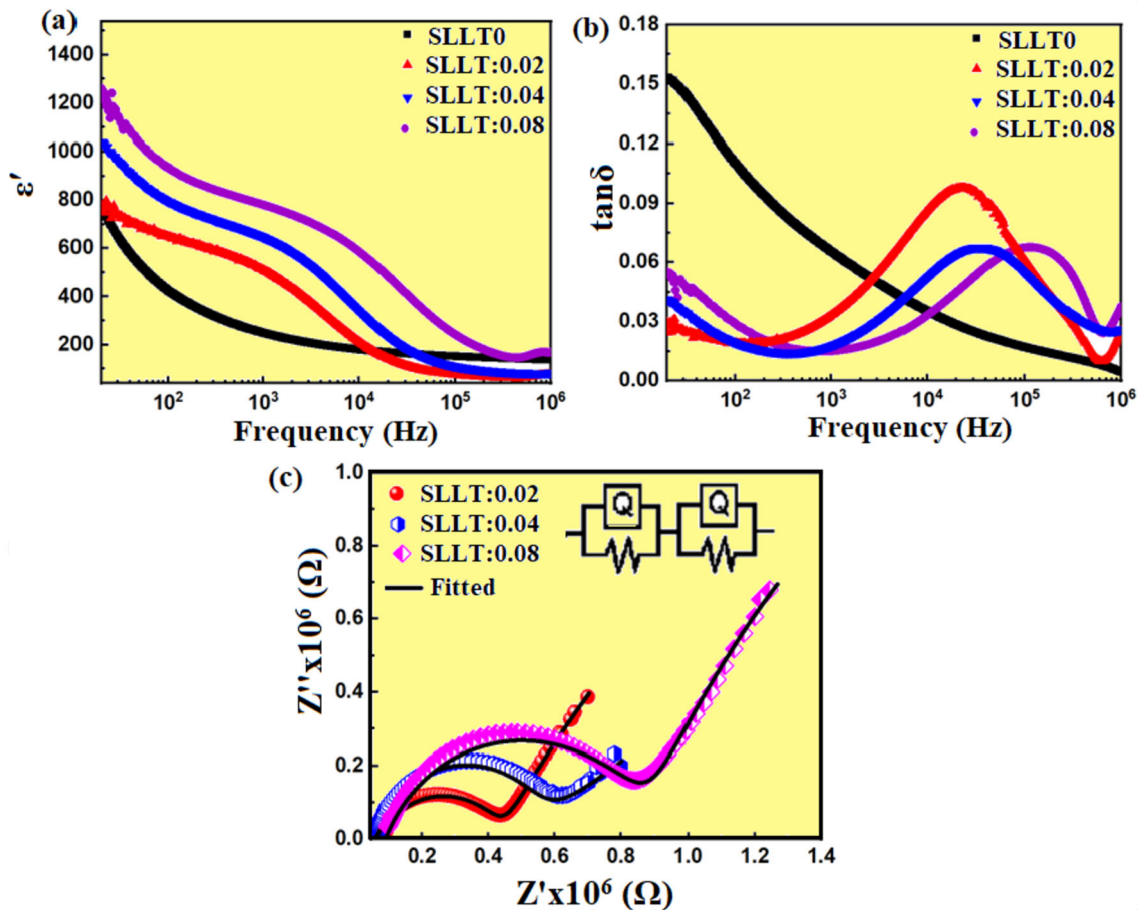


Fig. 6 a and b Frequency-dependent dielectric constant and dielectric loss and c Cole–Cole plots between Z' and Z'' for SLLT: x ceramics measured at room temperatures

an ideal equivalent circuit such as that inserted in Fig. 6c to fit the Z' & Z'' data as shown in Fig. 6c. This circuit consists of two parallel RC circuits coupled in series. One of these circuit components is for grain response, and the other is for grain boundary. The col-col plot, along with fitting, is shown in Fig. 6c. The codoped samples show two arcs in the diagram, suggesting relaxation behaviour in the present sample, as shown in Fig. 6a and b. The R_g , C_g , R_{gb} , and C_{gb} obtained from col-col plot fitting are reported in Table 2. It can be seen that the values of grain resistance are more significant than that of grain, suggesting the excellent insulation performance of the grain boundary. As the co-doping content increases, grain and grain boundary resistance increase, as shown in Fig. 6a and b. Also, increasing the resistance with co-doping can increase the breakdown voltage of the material, with is essential for energy storage applications.

Table 2 Cole–Cole plot output results, breakdown voltage, energy storage density, recoverable energy storage density, and energy storage efficiency of SLLT: x ceramics measured at room temperature

Sample	SLLT0	SLLT0.02	SLLT0.04	SLLT0.08
R_g (k Ω)	3.48E+04	5.23E+04	9.03E+04	3.48E+04
R_{gb} (k Ω)	3.48E+05	6.53E+05	1.00E+05	3.48E+05
C_g (F)	5.52E−08	1.14E−09	3.45E−08	5.52E−08
C_{gb} (F)	2.90E−10	7.69E−10	4.39E−10	2.90E−10
E_b (kv/cm)	249	254	262	270
W (J/cm ³)	0.76	1.257	2.024	2.696
W_{rec} (J/cm ³)	0.73	1.175	1.878	2.455
η (%)	96	93.47	92.79	91.06

3.5 Energy storage study

To investigate the energy storage property of SLLT: x ceramics, the polarization–electric field (P–E)

hysteresis loops were performed. The energy storage properties of SLLT:*x* ceramics are illustrated in Fig. 7. High P_{\max} , Low P_r , and high breakdown voltage are seen in the investigated ceramics in Fig. 7a, and b. The maximum polarization (P_{\max}) is approximately $10 \mu\text{C}/\text{cm}^2$ at a maximum applied electric field of $269.6 \text{ kV}/\text{cm}$ obtained for the sample SLLT0.08, which is about three times large that of the pure ST sample ($3.1 \mu\text{C}/\text{cm}^2$). This may be due to the more significant sum of average ionic polarizabilities of co-doping ions La^{3+} and Li^+ being more than the average ionic polarizability of Sr ions. Also, this increment in P_{\max} could be attributed to the increase in the density of the sample with co-doping. Interestingly, it can be seen that the breakdown strength of co-doped samples increases in comparison with pure models. Using the P–E loop and by integrating the area between the polarization axis and the discharge curve, as shown in Fig. 7c, and based on the

following equations, the energy storage density and energy storage efficiency (η) [66–71].

$$W = \int_0^{P_{\max}} E dp \tag{4}$$

$$W_{\text{rec}} = \int_{P_r}^{P_{\max}} E dp \tag{5}$$

$$\eta = \frac{W_{\text{rec}}}{W} = \frac{\int_{P_r}^{P_{\max}} E dp}{\int_0^{P_{\max}} E dp}, \tag{6}$$

where P_r denotes the remnant polarization, P_{\max} denotes the maximum polarization, and E is the electric field applied. High P_{\max} , low P_r , and high E_b are necessary to increase the energy storage density. The estimated values of W , W_{rec} and (η) are shown in

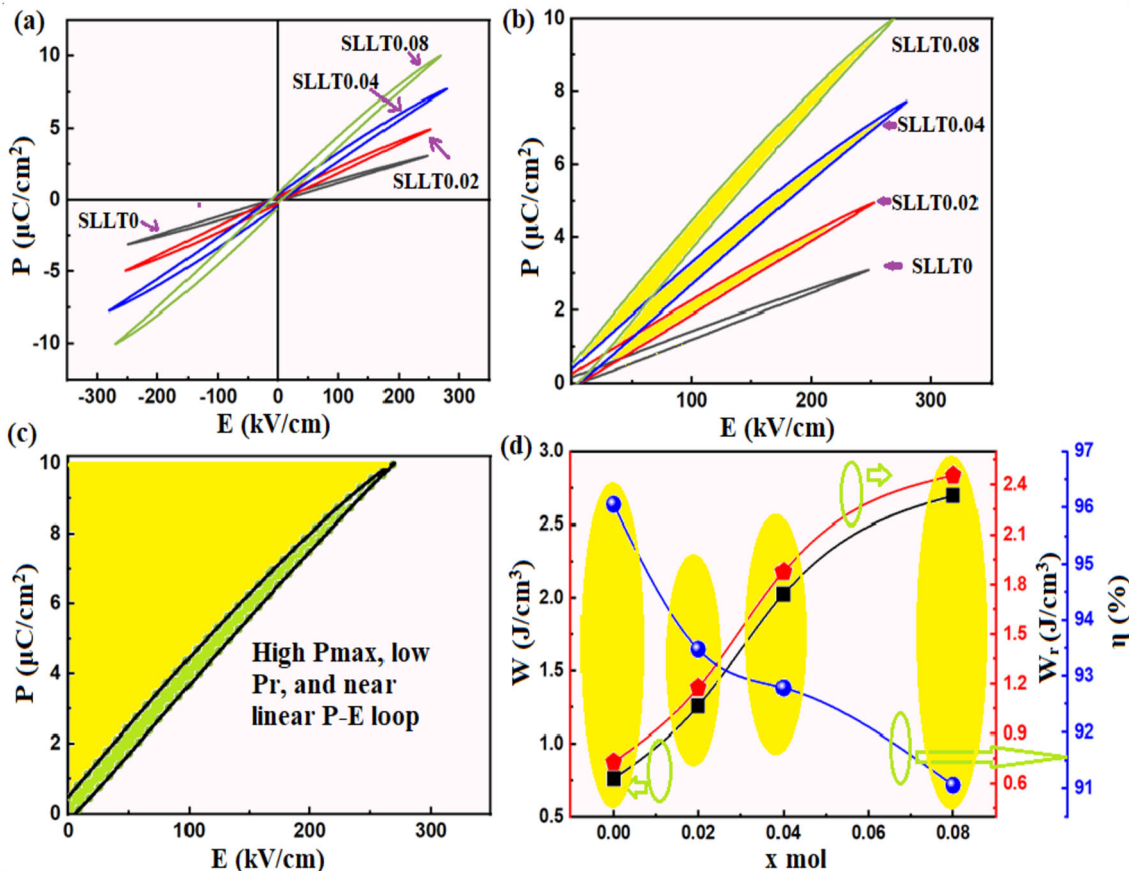


Fig. 7 a, b Room temperature P–E hysteresis loop (c). A representation of the positive part of the P–E loop, c a Schematic diagram for calculating the energy storage properties, and

d variation of energy storage density and energy storage efficiency with La^{3+} and Li^+ content

Fig. 7d. with the increase of La and Li concentration, the energy storage density increases while the energy efficiency (η) decrease. Interestingly, the study achieved a high energy storage density of > 2.5 and a high energy efficiency of $> 90\%$. As a result, the composition with $x = 0.08$ exhibits high breakdown strength of 279.6 kV, a low dielectric loss of 0.025 at 1 kHz, as well as an energy storage density of 2.75 J/cm³ and high energy efficiency of 91%, indicating that the La³⁺ and Li⁺ co-doped SrTiO₃ ceramics possess significant attributes for high power applications.

4 Conclusion

In summary Lead-free ceramic of La³⁺ and Li⁺ co-doped SrTiO₃ was successfully fabricated by solid-state reaction method. A single cubic phase was achieved in all sintered samples. The grain size was decreased with an increase in La and Li content. The obtained results revealed an increase in dielectric constant, breakdown voltage with an increase in the co-dopant content. The improvement can be attributed to the improved energy storage density. The enhanced dielectric breakdown strength is due to the reduced grain size and increased co-doping concentrations. Optimizing intrinsic and extrinsic factors (bulk structure defect chemistry and grain size) would improve dielectric breakdown strength, increase energy densities, and increase energy efficiency in commercially viable energy storage device capacitors for various applications. As a result, the composition with $x = 0.08$ exhibits high breakdown strength of 279.6 kV, a low dielectric loss of 0.025 at 1 kHz, as well as an energy storage density of 2.55 J/cm³ and high energy efficiency of 91%, indicating that the La³⁺ and Li⁺ co-doped SrTiO₃ ceramics possess significant attributes for high power applications.

Acknowledgements

The authors would like to acknowledge the experimental facilities provided by CNPq and FAPESP in Grupo de Materiais Ferroicos (GMF), Physics Department/ UFSCar. For financial support, Dr Alkathy is greatly indebted to the Sao Paulo Research Foundation (FAPESP: Grant no# 2019/03110-8) and (FAPESP: Grant no# 2017/13769-1).

Author contributions

All authors have contributed in preparation of the manuscript. MSA: Synthesis, Analysis and interpretation of the data, calculations, visualization, conceptualization, methodology, and writing-original draft. FLZ and FPM: Conceptualization, methodology, suggestions, and spectroscopic characterizations, and Prof JAE: supervision, writing, and approval of the final version.

Data availability

The data that support the findings of this study are available from the corresponding author on request.

Declarations

Conflict of interest The authors declare that they have no conflicts of interest.

Research involving human and animal rights This article does not contain any studies involving animal or human participants performed by any of the authors.

References

1. T.H. Chung, K.W. Kwok, *J. Alloys Compd.* **737**, 317–322 (2018)
2. M. Lun, W. Wang, Z. Xing, Z. Wan, W. Wu, H. Song, Y. Wang, W. Li, B. Chu, Q. He, *J. Am. Ceram. Soc.* **102**, 5243–5252 (2019)
3. X. Qiao, A. Sheng, D. Wu, F. Zhang, B. Chen, P. Liang, J. Wang, X. Chao, Z. Yang, *Chem. Eng. J.* **408**, 127368 (2021)
4. C. Jiang, L. Fang, M. Shen, F. Zheng, X. Wu, *Appl. Phys. Lett.* **94**, 071110 (2009)
5. J. Qi, M. Cao, Y. Chen, Z. He, C. Tao, H. Hao, Z. Yao, H. Liu, *J. Alloys Compd.* **772**, 1105–1112 (2019)
6. W. Pan, M. Cao, J. Qi, H. Hao, Z. Yao, Z. Yu, H. Liu, *J. Alloys Compd.* **784**, 1303–1310 (2019)
7. Y.B. Wang, W.J. Jie, C. Yang, X.H. Wei, J.H. Hao, *Adv. Funct. Mater.* **29**, 1808118 (2019)
8. G. Wang, Z. Lu, Y. Li, L. Li, H. Ji, A. Feteira, D. Zhou, D. Wang, S. Zhang, I.M. Reaney, *Chem. Rev.* **121**(10), 6124–6172 (2021)
9. L. Yang, X. Kong, F. Li, H. Hao, Z. Cheng, H. Liu, J. Li, S. Zhang, *Prog. Mater. Sci.* **102**, 72–108 (2019)
10. B. Zhong, Z. Long, C. Yang, Y. Li, X. Wei, *Ceram. Int.* **46**(12), 20565–20569 (2020)

11. M. Qin, F. Gao, J. Cizek, S. Yang, X. Fan, L. Zhao, J. Xu, G. Dong, M. Reece, H. Yan, *Acta Mater.* **164**, 76–89 (2019)
12. X. Guo, Y. Pu, W. Wang, L. Zhang, J. Ji, R. Shi, Y. Shi, M. Yang, J. Li, *ACS Sustain. Chem. Eng.* **7**(15), 13041–13052 (2019)
13. B. Wang, Y. Pu, Y. Shi, X. Guo, L. Zhang, L. Chang, J. Li, R. Li, J. Ji, T. Wei, *J. Am. Ceram. Soc.* **103**(12), 6811–6821 (2020)
14. X. Guo, Y. Pu, W. Wang, J. Ji, J. Li, M. Yang, R. Shi, *Ceram. Int.* **46**(10), 16644–16652 (2020)
15. J. Liu, Q. Liu, Z. Nie, S. Nie, D. Lu, P. Zhu, *Ceram. Int.* **45**(8), 10334–10341 (2019)
16. M. Qin, F. Gao, J. Cizek, S. Yang, X. Fan, L. Zhao, J. Xu, G. Dong, M. Reece, H. Yan, *Scripta Mater.* **190**, 118–120 (2021)
17. A. Tkach, O. Okhay, *Scr. Mater.* **190**, 38–39 (2021)
18. W. Pan, M. Cao, H. Hao, Z. Yao, Z. Yu, H. Liu, *J. Eur. Ceram.* **40**(1), 49–55 (2020)
19. M.S. Alkathy, K.J. Raju, J.A. Eiras, *J. Phys. D: Appl. Phys.* **54**(12), 125501 (2021)
20. A. Tkach, O. Okhay, *J. Mater. Sci. Technol.* **65**, 151–153 (2021)
21. B. Zhong, C. Zuo, C. Yang, S. Yang, Y. Li, H. Yu, X. Wei, *J. Alloys Compd.* **901**, 163556 (2022)
22. X. Zhu, P. Shi, R. Kang, S. Li, Z. Wang, W. Qiao, X. Zhang, L. He, Q. Liu, X. Lou, *Chem. Eng. J.* **420**, 129808 (2021)
23. Y. Pu, W. Wang, X. Guo, R. Shi, M. Yang, J. Li, *J. Mater. Chem. C* **7**, 14384–14393 (2019)
24. W. Pan, M. Cao, A. Jan, H. Hao, Z. Yao, H. Liu, *J. Mater. Chem. C* **8**, 2019–2027 (2020)
25. X. Guo, Y. Pu, W. Wang, J. Ji, J. Li, R. Shi, M. Yang, *Ceram. Int.* **46**, 21719–21727 (2020)
26. J. Zhang, K. Tse, M. Wong et al., A brief review of co-doping. *Front. Phys.* **11**, 117405 (2016)
27. K.M. Batoo, R. Verma, A. Chauhan, R. Kumar, M. Hadi, O.M. Aldossary, Y. Al-Douri, *J. Alloys Compd.* **883**, 160836 (2021)
28. K. Wu, H. Wang, Z. Miao, S. Ding, Y. Qi, Y. Ming, W. Ding, H. Yuan, Q. Zheng, D. Lin, *Ceram. Int.* **46**(9), 13159–13169 (2020)
29. F. Zeng, M. Cao, L. Zhang, M. Liu, H. Hao, Z. Yao, H. Liu, *Ceram. Int.* **43**(10), 7710–7716 (2017)
30. W. Pan, M. Cao, A. Jan, H. Hao, Z. Yao, H. Liu, *J. Mater. Chem. C* **8**(6), 2019–2027 (2020)
31. C. Wang, F. Yan, H. Yang, Y. Lin, T. Wang, *J. Alloys Compd.* **749**, 605–611 (2018)
32. A. Jan, H. Liu, H. Hao, Z. Yao, M. Emmanuel, W. Pan, A. Ullah, A. Manan, A. Ullah, M. Cao, A.S. Ahmad, *J. Alloys Compd.* **830**, 154611 (2020)
33. T. Li, P. Chen, F. Li, C. Wang, *Chem. Eng. J.* **406**, 127151 (2021)
34. L. Zheng, P. Sun, P. Zheng, W. Bai, L. Li, F. Wen, J. Zhang, N. Wang, Y. Zhang, *J. Mater. Chem. C* **9**(15), 5234–5243 (2021)
35. H. Yang, J. Tian, Y. Lin, J. Ma, *Chem. Eng. J.* **418**, 129337 (2021)
36. Y. Fang, M. Cao, Z. He, W. Pan, H. Wang, Z. Yao, H. Hao, H. Liu, *J. Mater. Sci.: Mater. Electron.* **31**(16), 13408–13414 (2020)
37. P. Zhao, Z. Fang, X. Zhang, J. Chen, Y. Shen, X. Zhang, Q. An, C. Yang, X. Gao, S. Zhang, B. Tang, *ACS Appl. Mater. Interface* **13**, 24833–24855 (2021)
38. L. Cao, Y. Yuan, E. Li, S. Zhang, *Ceram. Int.* **45**(5), 5660–5667 (2019)
39. Z. Yang, Y. Yuan, L. Cao, E. Li, S. Zhang, *Ceram. Int.* **46**(8), 11282–11289 (2020)
40. X. Kong, L. Yang, Z. Cheng, S. Zhang, *J. Am. Ceram. Soc.* **103**(3), 1722–1731 (2020)
41. L.L. Liu, B.K. Chu, P. Li, P. Fu, J. Du, J.G. Hao, W. Li, H.R. Zeng, *Chem. Eng. J.* **429**, 132548 (2022)
42. M.V. Le et al., *Catalysts* **11**(5), 564 (2021)
43. R.D. Shannon, *Acta Cryst. A* **32**, 751–767 (1976)
44. U. Holzwarth, N. Gibson, *Nat. Nanotechnol.* **6**, 534–534 (2011)
45. V.D. Mote, Y. Purushotham, B.N.J. Dole, *Theor. Appl. Phys.* **6**(1), 1–8 (2012)
46. M.S. Alkathy, K.K. Bokinala, K. James Raju, C. J. Mater. Sci.: Mater. Electron. **27**(4), 3175–3181 (2016)
47. M.S. Alkathy, K.C.J. Raju, *Mater. Sci.: Mater. Electron.* **27**(9), 8957–8965 (2016)
48. K. Madhan, R. Murugaraj, *Appl. Phys. A* **126**(2), 1–12 (2020)
49. A.K. Yadav, H. Fan, B. Yan et al., *J. Mater. Sci. Mater. Electron.* **32**, 23103–23115 (2021)
50. A.K. Yadav, A. Verma, S. Kumar, V. Srihari, A.K. Sinha, V.R. Reddy, S.W. Liu, S. Biring, S. Sen, *J. Appl. Phys.* **123**, 2124102 (2018)
51. R.C. Hatch, K.D. Fredrickson, M. Choi, C. Lin, H. Seo, A.B. Posadas, A.A. Demkov, *J. Appl. Phys.* **114**(10), 103710 (2013)
52. B. Erdem, R.A. Hunsicker, G.W. Simmons, E.D. Sudol, V.L. Dimonie, M.S. El-Aasser, *Langmuir* **17**(9), 2664–2669 (2001)
53. L. Li, T. Lu, N. Zhang, J. Li, Z.J. Cai, *Mater. Chem. C* **6**(9), 2283–2294 (2018)
54. M.S. Alkathy, F.L. Zabotto, K.J. Raju, J.A. Eiras, *Mater. Chem. Phys.* **275**, 125235 (2022)
55. M.S. Alkathy, F.L. Zabotto, F.P. Milton, J.A. Eiras, *J. Alloys Compd.* **908**, 164222 (2022)
56. Y. Lee, C.H. Lee, T. Nam, S. Lee, I.K. Oh, J.Y. Yang, D.W. Choi, C. Yoo et al., *J. Mater. Sci.* **54**(16), 11145–11156 (2019)

57. N. Hornsvelde, B. Put, W.M. Kessels, P.M. Vereecken, M. Creatore, Plasma-assisted and thermal atomic layer deposition of electrochemically active Li_2CO_3 . *RSC Adv.* **7**(66), 41359–41368 (2017)
58. M. Ganguly, S.K. Rout, T.P. Sinha, S.K. Sharma, H.Y. Park, C.W. Ahn, I.W. Kim, *J. Alloys Compd.* **579**, 473 (2013)
59. M. Rizwan, I. Zeba, M. Shakil, S.S. Gillani, Z. Usman, *Optik* **211**, 164611 (2020)
60. A.J. Moulson, J.M. Herbert, *Electroceramics: Materials, Properties and Applications* (Chapman and Hall, London, 1990), p. 24
61. S.K. Ghosh, M. Ganguly, S.K. Rout, T.P. Sinha, *Eur. Phys. J. Plus* **130**(4), 1–18 (2015)
62. M. Soni, M. Saleem, N. Bajpai, S. Chouhan, M.D. Varshney, A. Mishra, *AIP Conf. Proc.* **2100**, 020185 (2019)
63. M.S. Alkathy, J.A. Eiras, K.J. Raju, *Ferroelectrics* **570**(1), 153–161 (2021)
64. Z. Liang, M. Liu, C. Ma, L. Shen, L. Lu, C.L. Jia, *J. Mater. Chem. A* **6**(26), 12291–12297 (2018)
65. X. Jiang, D. Wang, M. Sun, N. Zheng, S. Jia, H. Liu, D. Zhang, W. Li, *RSC Adv.* **7**(79), 49962–49968 (2017)
66. A. Kumar, S.H. Kim, M. Peddigari et al., *Electron. Mater. Lett.* **15**, 323–330 (2019)
67. N. Qu, H. Du, X. Hao, *J. Mater. Chem. C* **7**(26), 7993–8002 (2019)
68. A. Kumar, J.Y. Yoon, A. Thakre, M. Peddigari, D.Y. Jeong, Y.M. Kong, J. Ryu, *J. Korean Ceram. Soc.* **56**(4), 412–420 (2019)
69. Z. Yao, Q. Luo, G. Zhang, H. Hao, M. Cao, H.J. Liu, *Mater. Sci.: Mater. Electron.* **28**(15), 11491–11499 (2017)
70. A. Kumar, G. Lee, Y.G. Chae, A. Thakre, H.S. Choi, G.H. Nam, J. Ryu, *Ceram. Int.* **47**(22), 31590–31596 (2021)
71. A. Kumar, S.H. Kim, A. Thakre, G. Lee, Y.G. Chae, J. Ryu, *J. Therm. Spray Technol.* **30**(3), 591–602 (2021)

Publisher's Note Springer Nature remains neutral with regard to jurisdictional claims in published maps and institutional affiliations.